eprints@whiterose.ac.uk
https://eprints.whiterose.ac.uk/

Binary Solvent System Used to Fabricate Fully Annealing-Free Perovskite Solar Cells

Elena J. Cassella,* Emma L.K. Spooner, Joel A. Smith, Timothy Thornber, Mary E. O'Kane, Robert D.J. Oliver, Thomas E. Catley, Saqlain Choudhary, Christopher J. Wood, Deborah B. Hammond, Henry J. Snaith, and David G. Lidzey*

High temperature post-deposition annealing of hybrid lead halide perovskite thin films—typically lasting at least 10 min—dramatically limits the maximum roll-to-roll coating speed, which determines solar module manufacturing costs. While several approaches for "annealing-free" perovskite solar cells (PSCs) have been demonstrated, many are of limited feasibility for scalable fabrication. Here, this work has solvent-engineered a high vapor pressure solvent mixture of 2-methoxy ethanol and tetrahydrofuran to deposit highly crystalline perovskite thin-films at room temperature using gas-quenching to remove the volatile solvents. Using this approach, this work demonstrates p-i-n devices with an annealing-free MAPbI$_3$ perovskite layer achieving stabilized power conversion efficiencies (PCEs) of up to 18.0%, compared to 18.4% for devices containing an annealed perovskite layer. This work then explores the deposition of self-assembled molecules as the hole-transporting layer without annealing. This work finally combines the methods to create fully annealing-free devices having stabilized PCEs of up to 17.1%. This represents the state-of-the-art for annealing-free fabrication of PSCs with a process fully compatible with roll-to-roll manufacture.

1. Introduction

Organic–inorganic metal halide perovskites are rapidly approaching state-of-the-art silicon solar cells, with best-performing devices now reaching power conversion efficiencies (PCEs) of 25.7%.[1] Although stability remains a challenge for perovskite solar cells (PSCs), their solution-processability represents a major advantage. Techniques such as blade coating,[2] slot-die coating,[3] and spray coating[4] are compatible with roll-to-roll (R2R) processing, which—in principle—should allow much higher throughput speeds than existing silicon solar technologies. However, the lengthy annealing times used to crystallize the perovskite active layer reduce the maximum theoretical web speeds that could be achieved in a practical manufacture process.

In 2020, Rolston et al. demonstrated the highest coating speeds of any scalable PSC processing technologies, achieving production speeds of >12 m min^{-1}.[5] Spray coating was combined with an atmospheric plasma postprocessing route,[6] creating PSC devices and modules with a PCE of 18% and 15.5%, respectively. Critically, these were fabricated without annealing the perovskite layer. At these speeds, the module cost is expected to be fully competitive with Si.[7] In contrast, the calculated throughput rate for spin-coated PSCs incorporating a 10-min anneal is just 0.017 m min^{-1}; a rate prohibitive for commercialization. Furthermore, high temperature processing steps increase device manufacturing costs through increased utility costs and reduced throughput.[8] High process temperatures are also incompatible with many sensitive flexible (polymeric) substrates that are expected to be important in "Internet of Things" applications.[9,10] This growing market is expected to reduce the initial investment and barrier to market entry for perovskites by an order of magnitude.[11]

Many approaches to create "annealing-free" PSCs have been demonstrated. For example, thermal evaporation of the perovskite layer without any post-annealing treatments can be used to realize devices having reasonable PCEs of up to 15.7%.[12,13] Zhou et al. demonstrated devices with a PCE of 15.7% for MAPbI$_3$ (where MA is methylammonium) films grown via electrochemical fabrication.[14] The use of antisolvent

E. J. Cassella, E. L. K. Spooner, T. Thornber, M. E. O'Kane,
R. D. J. Oliver, T. E. Catley, D. G. Lidzey
Department of Physics and Astronomy
University of Sheffield
Sheffield S3 7RH, UK
E-mail: e.j.cassella@sheffield.ac.uk; d.g.lidzey@sheffield.ac.uk
J. A. Smith, S. Choudhary, H. J. Snaith
Department of Physics
University of Oxford
Clarendon Laboratory
Parks Road, Oxford OX1 3PU, UK
C. J. Wood
Power Roll Limited
Unit 5 Jade Business Park, Spring Road, Seaham SR7 9DR, UK
D. B. Hammond
Department of Chemistry
University of Sheffield
Sheffield S3 7HF, UK

**ADVANCED
SCIENCE NEWS**

www.advancedsciencenews.com

**ADVANCED
ENERGY
MATERIALS**

www.advenergymat.de

treatments is an effective way to rapidly remove highly coordinating solvents, such as dimethylformamide, dimethyl sulfoxide, n-methyl-2-pyrrolidone, and dimethylacetamide (DMF, DMSO, NMP, and DMAc, respectively), and crystallize the perovskite at room temperature.[15–20] Although efficiencies of up to 20.1% have been achieved[21] using such processes, antisolvent treatments are difficult to use at scale due to the large volume of mostly toxic washing solvents that become increasingly contaminated. Ultrasonic vibration-based posttreatments have also been used in conjunction with high-boiling point (low vapor pressure) solvents.[22] Notably, $(FAPbI_3)_{0.85}(MA PbBr_3)_{0.15}$ compositions, where FA is formamidinium, can be created at room temperature via this route.[23,24] Perovskite crystallization has also been generated by exposing two-step, spin-coated $MAPbI_3$ films to humid air, with devices having a PCE of >15% demonstrated, however this process required an exposure time of an hour.[25] Dubey et al. adapted this process,[26] to make spin-coated perovskite films from a low vapor pressure mix of GBL (gamma-butyrolactone) and DMSO which were then exposed to an antisolvent wash followed by exposure to humid air. This approach created devices with efficiencies of up to 16.8% after 5 h of air-exposure.

The use of volatile solvent systems has been identified as an extremely promising alternative route for the scalable fabrication of PSCs. Such processes can eliminate complex post-deposition treatments to remove highly coordinating, non-volatile solvents.[27] The use of high vapor pressure, low boiling point solvents enables rapid evaporation of the casting solvent, and significantly reduces the time required to induce a high degree of supersaturation and crystal nucleation. A number of volatile solvents have now been explored for posttreatment-free fabrication of PSCs, including DMF,[28] acetonitrile (ACN),[29] mixtures of methylamine in tetrahydrofuran (THF) or ethanol (EtOH) in combination with a secondary solvent (ACN,[30] or THF[31]), and 2-methoxyethanol[32] (2-ME). We note that 2-ME has recently emerged[33] as an excellent solvent for PSC fabrication due to its low boiling point. High-performance PSCs have now been fabricated from 2-ME using a number of techniques, including blade coating,[34,35] bar coating,[36,37] slot-die coating,[38] and spray coating.[39]

Here, we use a mixture of 2-ME with THF as a route to deposit highly crystalline $MAPbI_3$ perovskite films without the requirement for any posttreatment heating steps. The process developed uses gas-quenching to accelerate the evaporation of the volatile casting solvents to induce a high degree of nucleation, with dense, pinhole-free perovskite films created. Devices fabricated in this manner demonstrate PCEs of up to 18%. We then demonstrate that a carbazole-based self-assembled monolayer (SAM) can also be deposited and used as a hole-transporting layer (HTL) without the necessity for annealing. These carbazole-based SAMs are a very promising HTL for p-i-n PSCs:[40] tandem devices incorporating a carbazole-based SAM demonstrated a PCE > 29%,[41] while single junction devices have demonstrated a PCE > 22%[42] and excellent stability.[43] Further, the SAMs have been successfully deposited via scalable methods such as slot-die coating[38] and spray coating.[39]

Using these approaches, we create fully "annealing-free" PSCs achieving stabilized PCEs of up to 17.1%. To our knowledge, this number represents the highest literature value for a fully annealing-free PSC device having no additional

post-processing steps, making our process compatible with high-throughput R2R coating. We expect that such a fully R2R-compatible processes will have a high degree of industrial-relevance, eliminating energy-expensive, time-consuming heating steps which will limit manufacturing throughput. Our process also avoids the use of any toxic antisolvents which are difficult to use at scale.

2. Results and Discussion

2.1. Optimization of the Casting Precursor Solution Composition for High Device Efficiency

We have explored the use of THF as a high vapor pressure additive in a 2-ME $MAPbI_3$ precursor ink to facilitate fast solvent drying and formation of a crystalline perovskite at room temperature. According to Raoult's law, the total vapor pressure of a system is a function of the partial vapor pressures of the components in a mixture.[44] For ideal mixtures, the total vapor pressure of a mixture will linearly increase (decrease) upon the addition of a higher (lower) vapor pressure component. In reality however, nonideal behavior will arise from interactions between molecules in solution, resulting in a deviation from ideal, linear behavior. The vapor pressures of THF and 2-ME are 162 and 9.5 mm Hg at 25 °C, respectively.[45,46] Assuming negligible molecular interactions, we might expect the rapid evaporation of the volatile THF solvent to accelerate the saturation of a precursor film, which in turn results in the onset of crystallization. The rapid drying of such a wet film should produce compact layers which are comprised of smaller crystals. Such high-quality perovskite thin films would ideally not contain any residual solvent and would not need annealing. Here, we note that Zhang et al. recently employed THF as a cosolvent in a DMF:DMSO precursor ink to fabricate annealed PSC devices with PCEs of up to 24%.[47]

In our experiments, we screened 11 compositions of THF and 2-ME from 0 to 100 vol% of THF cosolvent in steps of 10 vol%. For simplicity, we use a naming convention that refers to the solvent ratio of THF:2-ME, i.e., 0:10 for a 0 vol% THF composition. Images of $MAPbI_3$ solutions with a molarity of 0.5 M for each composition are shown in Figure S1 (Supporting Information). It can be seen that for compositions >70 vol% THF, the precursor materials were not solubilized, instead black $MAPbI_3$ was precipitated. Such precipitated solutions are not suitable for perovskite thin-film fabrication and so were not studied further.

The solubility limit is indicative of reduced coordination between the THF and the Pb^{2+} and I^- moieties in solution. In a $MAPbI_3$ solution, an equilibrium mixture of solvent molecules and I^- ligands will be reached that will depend on the affinity between the solvents and each ion (MA^+, I^-, Pb^{2+}), in the Pb^{2+} first coordination sphere. The resulting PbI_x^{2-x+} polyiodide plumbate complexes have characteristic absorption bands, so I^- and Pb^{2+} interactions can be used to understand the competing interactions between the solvents and the solvated ions. To do this, we have measured the ultraviolet (UV) visible transmittance of dilute (0.05 M) inks having different THF:2-ME compositions. The corresponding absorbances over the
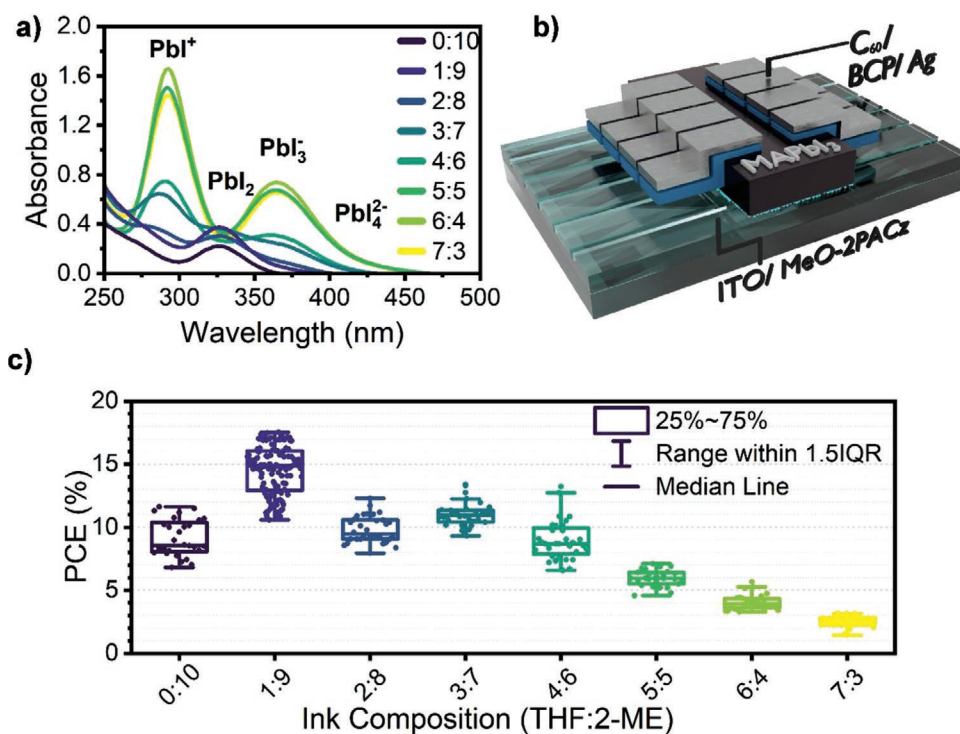
ADVANCED
SCIENCE NEWS
www.advancedsciencenews.com

ADVANCED
ENERGY
MATERIALS
www.advenergymat.de

Figure 1. a) The absorbance spectra of MAPbI$_3$ in each of the tetrahydrofuran (THF):2-methoxyethanol (2-ME) precursor ink compositions. b) An illustrative schematic of the p-i-n device architecture used. c) The corresponding device power conversion efficiency (PCE) of cells containing an absorber layer fabricated from each ink composition.

wavelength range 250–500 nm are shown in **Figure 1**a. Here, the PbI$^+$, PbI$_2$, PbI$_3^-$, and PbI$_4^{2-}$ labels correspond to decreasing numbers of coordinated solvent ligands, i.e., PbI$^+$Solv$_5$, PbI$_2$Solv$_4$, PbI$_3^-$Solv$_3$, and PbI$_4^-$Solv$_2$, respectively.[48,49] Upon addition of THF, there is a clear increase in absorbance by higher-order iodoplumbate species compared to pure 2-ME solutions. Indeed, solutions based on a 2-ME solvent exhibit absorption peaks corresponding to PbI$^+$Solv$_5$ ($\approx$270 nm) and PbI$_2$Solv$_4$ (326 nm) alone. Conversely, the addition of THF results in the formation of PbI$_3^-$Solv$_3$ (365 nm), and PbI$_4^{2-}$Solv$_2$ (420 nm) species at >50 vol% of THF.

Interestingly, the observed trend does not follow that predicted by the donor numbers, D_N, of 2-ME and THF. Here, D_N describes the strength of the interaction between a Lewis-basic solvent and soft Lewis-acidic Pb^{2+} centers. In solvents with low D_N, the I$^-$ to Pb^{2+} ligand interaction dominates rather than solvent coordination, shifting the equilibrium toward higher order PbI$_x^{2-x+}$ complexes.[50] The D_N values for THF and 2-ME are very similar, being 20.0[51] and 19.7,[52] respectively. Despite the nominally near-identical affinity to Pb^{2+} ions, we instead attribute the formation of higher-order polyiodide plumbates in THF to reduced hydrogen bonding interactions. Indeed, the greater the Hansen hydrogen-bonding parameter, δ_{HB}, the stronger the interaction between the solvent and organic cations and halide anions in solution.[53] The δ_{HB} values for THF and 2-ME are 8.0 and 16.4, respectively.[54] This suggests therefore, that the 2-ME (THF) should solvate the methylammonium and iodide species to a greater (lesser) extent, precluding (facilitating) coordination of I$^-$ to the Pb^{2-} ions.

It has been speculated that higher order iodoplumbate complexes, meaning more highly halide-coordinated Pb, promote the transformation of the precursor to the perovskite phase, for example through the formation of larger and more oriented perovskite crystals.[48,55,56] Indeed, the relatively weak coordination of both 2-ME and THF to Pb^{2+} is expected to suppress the formation of solvent-coordinated intermediates which would require thermal annealing for solvent dissociation.

To evaluate the performance of the various precursor inks, we fabricated a series of photovoltaic devices. All devices were fabricated on cleaned, patterned indium tin-oxide (ITO) coated glass substrates, with all processing performed within an N$_2$-filled glovebox. An MeO-2PACz ([2-(3,6-dimethoxy-9H-carbazol-9-yl)ethyl]phosphonic acid)[40] HTL was first spin-coated and—in initial studies—was annealed at 100 °C for 10 min. The MAPbI$_3$ perovskite precursor inks were then spin-coated and "gas-quenched" by directing a flow of N$_2$ at the spinning substrate to promote evaporation of the volatile solvents. Gas-quenching is a facile, low-cost technique that has been demonstrated to have excellent potential for large-area PSC fabrication.[57] An immediate color change from yellow to dark brown was observed upon application of the gas-jet for all ink compositions. The converted perovskite films were not annealed. The substrates were then transferred to an evaporation chamber for deposition of a C$_{60}$/bathocuproine (BCP) electron-transporting layer (ETL) and an Ag cathode. Figure 1b shows a schematic of the p-i-n device architecture used. All processes and techniques are described fully in the Experimental Section.
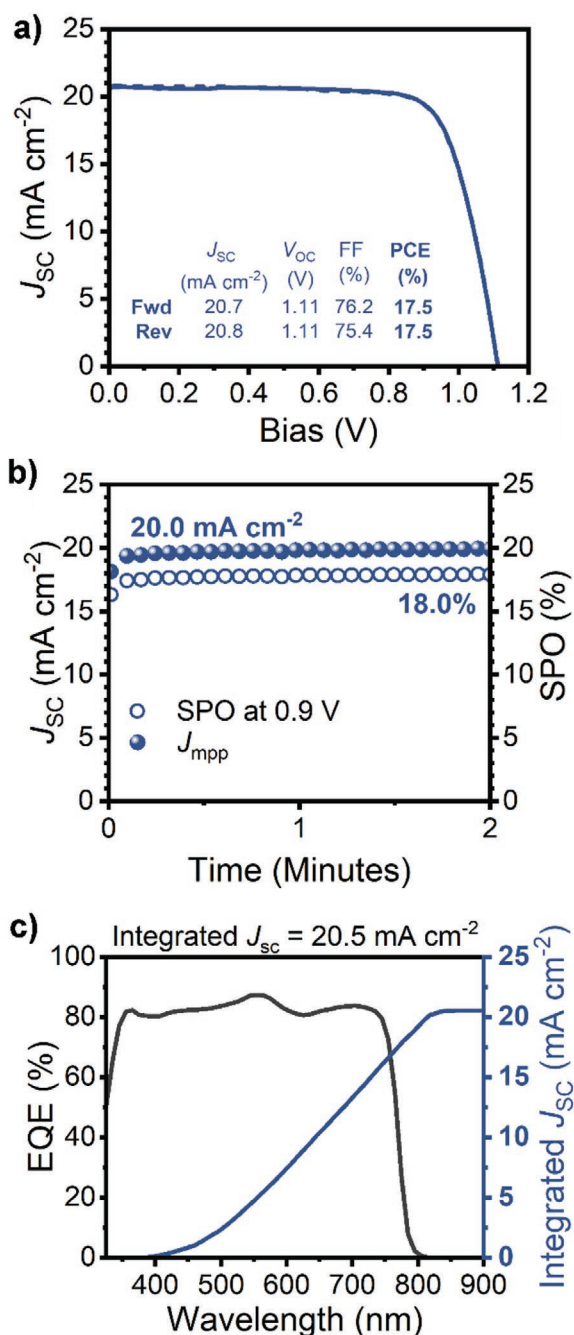
**ADVANCED
SCIENCE NEWS**

www.advancedsciencenews.com

**ADVANCED
ENERGY
MATERIALS**

www.advenergymat.de

a)

b)

c)

Figure 2. a) J–V curve, b) stabilized power output (SPO), and c) external quantum efficiency (EQE) of the best-performing cell with an annealing-free perovskite absorber layer fabricated from the 1:9 ink composition.

Figure 1c shows a boxplot of the resulting device PCEs for the range of compositions of THF:2-ME from 0:10 to 7:3. It can be seen that there is a significant variation in device performance. Here, it is found that devices fabricated from 10 vol% THF have a median PCE of 14.9% which is substantially higher than for devices made from a pure 2-ME solution, which have a median PCE of 8.6%. Devices made from 20 vol% < V_{THF} < 40 vol% solutions have a very similar efficiency compared to the pure 2-ME precursor devices. At >50 vol% THF, device performance

is significantly reduced. This trend is similar for other device metrics (short-circuit current density (J_{SC}), open-circuit voltage (V_{OC}), and fill factor (FF)) as shown in Figure S2 (Supporting Information).

Using the optimum 1:9 THF:2-ME composition, we demonstrate devices having stabilized PCEs of up to 18.0%. The current–density (J–V) curve, 2-min stabilized power output (SPO), and corresponding external quantum efficiency (EQE) graph are presented in **Figure 2**a–c, respectively. This champion device displays negligible hysteresis and has a J_{SC} of 20.8 mA cm^{-2}, a V_{OC} of 1.11 V, a FF of 75.4%, and PCE of 17.5% determined from the reverse sweep. An integrated J_{SC} of 20.5 mA cm^{-2} determined from the EQE curve ($J_{\text{SC-EQE}}$) is also in good agreement with the measured $J_{\text{SC-JV}}$.[58] Note that we determine a positive light-soaking effect, resulting in a SPO of 18.0%. This value compares favorably with the state-of-the-art annealing-free devices, and occurs without the use of any antisolvents, prepurification of any precursor materials, or preheating of the substrate or solution.

To benchmark the performance of the THF:2-ME solvent system against a prototypical solvent system used in PSC fabrication, we have investigated a methylamine and ACN precursor solution.[59,60] ACN also has a high vapor pressure (≈73 mm Hg[59]) and so provides a representative comparison to the THF:2-ME system. In Figure S3 (Supporting Information), we present a statistical summary of the device performance for cells incorporating an annealing-free perovskite active layer cast from the ACN/methylamine system against those cast from the annealing-free 1:9 solvent composition. We find that the median (champion) performance of the ACN-based devices is 11.2% (13.9%, n = 20); a performance that is notably lower than the 14.9% (17.5%, n = 62) demonstrated using the THF:2-ME solvent system.

To investigate the beneficial effect of incorporating 10 vol% THF, we have conducted several characterization studies. Firstly, to investigate the influence of the THF:2-ME ratio on the structure of the resulting perovskite thin-films, we recorded X-ray diffractograms (XRD) of films cast from each solvent composition which we display in **Figure 3**a. It can be seen that films cast from each solvent compositions display the characteristic peaks of MAPbI$_3$.[61] Importantly, we do not observe any crystalline intermediate residues in the diffraction patterns. This implies that the gas-quench successfully converts the precursor into a highly crystalline film for all compositions of THF:2-ME. Figure 3b shows the full width at half-maximum (FWHM) of the (110)/(002) perovskite peak at ≈14.2°. Here, it can be seen that the linewidth broadens with increasing proportions of THF. The linewidth can be used as a marker for crystallite size,[62] which suggests that smaller crystallites are formed from inks containing an increasing proportion of THF. This finding is consistent with a greater density of nuclei being formed in precursor films containing a higher vapor pressure, less-coordinating precursor solvent.

We have measured the thickness of the spin-coated films fabricated from each ink composition, as shown in Figure 3c. Here, a large increase in both the film thickness and standard deviation of the data is observed, going from 276 ± 14.0 nm (standard deviation, n = 5) for films cast from the 0:10 ink, to 586 ± 101 nm for the films cast from the 7:3 solvent ratio. To
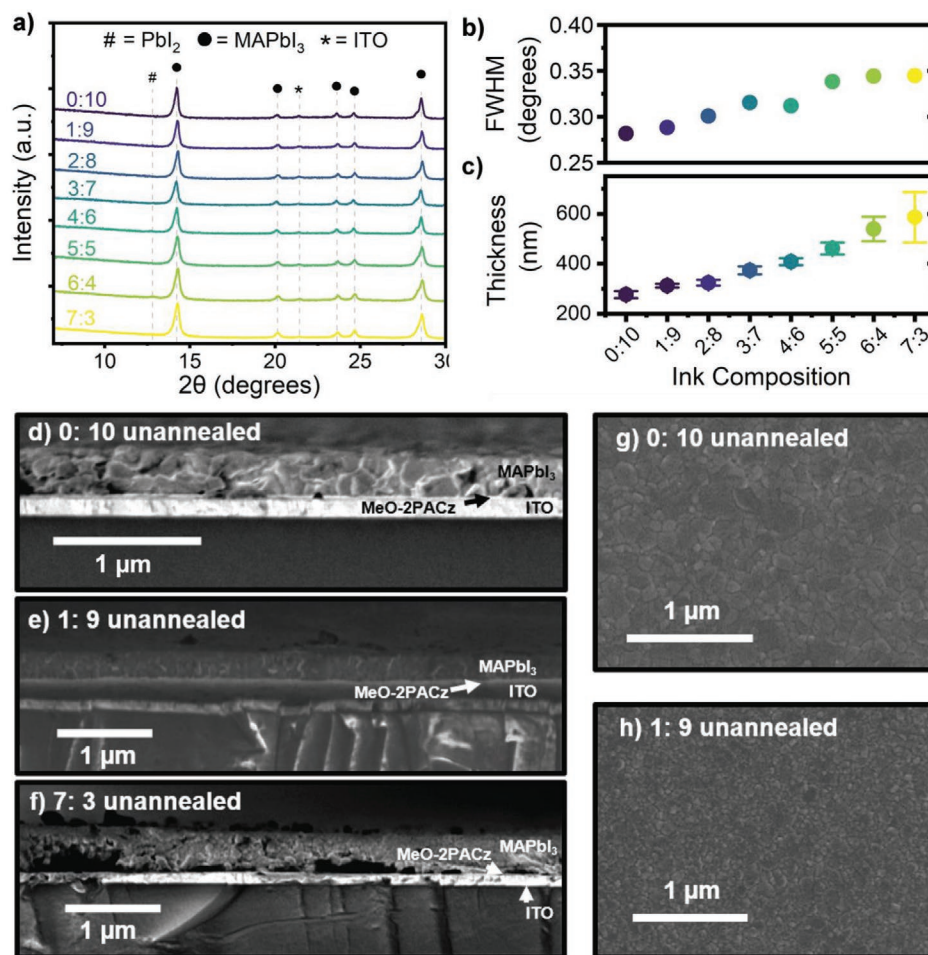
Figure 3. a) X-ray diffraction (XRD) patterns of perovskite films fabricated from each ink composition. b) The extracted full-width-at-half-maximum of the perovskite diffraction peak at ≈14.2 ° 2θ. c) The thickness of the perovskite absorber layer fabricated from each ink composition. Cross-sectional scanning electron microscope (SEM) images of perovskite films fabricated from the d) 0:10 precursor, e) 1:9 precursor, and f) 7:3 precursor ink. Top-down SEM images of perovskite films fabricated from g) 0:10 precursor ink and h) 1:9 precursor ink.

investigate the effect of the THF:2-ME ratio on perovskite morphology, we recorded both optical microscope images and scanning electron microscope (SEM) images. It is known that voids can form within films due to the solidification of the top surface induced by a gas-jet.[34] Such rapid solvent evaporation is expected to be exacerbated by high proportions of the more volatile THF component. This effect has been previously reported in perovskite films fabricated from volatile precursors.[34] Voids in the perovskite films reduce the working area of the device, reducing initial performance, act as regions of high recombination, and have been identified as regions from which degradation of the perovskite film is initiated.[35] Figure S4a–h (Supporting Information) shows optical microscope images of a series of films cast from the different precursor solutions. Here, it can be seen that there is a reduction in surface uniformity with increased THF concentration. Indeed, the film fabricated from the 7:3 ink is characterized by a number of large pinholes visible in the top surface of the film. We have used atomic force microscopy (AFM) to quantify the surface roughness of films cast from each solvent composition. Figure S5a–h (Supporting Information) shows 5 × 5 µm AFM images of films

cast from each composition. In Figure S5i (Supporting Information) we plot the average (n = 3) root-mean-square roughness (Rq) of film cast from each composition. It can be seen that there is an increase in the Rq of the perovskite films cast from the precursor inks with >40 vol% THF. This quantitative trend in the roughness is in agreement with the decreased surface uniformity seen in the optical microscope images in the Figure S4 (Supporting Information). We speculate that the apparent decrease in surface roughness between the 1:9 and 3:7 compositions arise from a reduction in grain size, leading to a smoother, more densely packed film morphology.

In Figure 3d–f we present cross-sectional SEM images of films fabricated from the 0:10, 1:9 (champion), and 7:3 inks. Here, it is clear that there a number of voids between the perovskite crystal grains within the film cast from pure 2-ME (0:10, see Figure 3d). We speculate that these result from regions of trapped solvent caused by the high boiling point of pure 2-ME. Upon annealing, this trapped solvent is expected to rapidly escape through the top surface of the film, creating pinholes throughout the perovskite layer; a finding consistent with previous reports.[38] For films cast from the 1:9 ink—which

resulted in the highest device PCEs—these voids appear largely absent, with good contact made between the perovskite layer and the substrate surface, as seen in Figure 3e. In contrast, at 70 vol% THF, we observe large voids at the perovskite:substrate interface (see Figure 3f). The perovskite film thicknesses determined from the SEM cross-sectional images correspond well to those presented in Figure 3c which were measured using surface profilometry. It can be seen that the interfacial voids in films cast from solutions containing a higher concentration of THF contribute to the enhanced film "thickness" as measured between the upper surface of the perovskite film and the underlying ITO interface.

Our SEM images of the top-surface of films cast from 0:10 and 1:9 precursor solutions indicate that there is a reduction in the grain size upon addition of THF to the precursor (see Figure 3g,h, with the full images presented in Figure S6a,b, Supporting Information). While a number of pinholes are observed in the top-surface of the film cast from the 0:10 ink, only one such defect is seen in the top-surface of the film cast from the 1:9 solution. To track the effect of increased THF incorporation on the film morphology, we have recorded SEM images of the top surface of films cast from 3:7, 5:5, and 7:3 THF:2-ME solvent compositions (see Figure S7, Supporting Information). Here, it is apparent that films cast from each composition are characterized by small grains. For the film cast from the 7:3 solution, a number of pinholes are again observed in the upper surface. Our results suggest therefore, that 10 vol% THF in the 2-ME precursor solution allows the creation of a compact film of small MAPbI$_3$ crystallites without pinholes and with excellent contact to the underlying substrate. At higher THF concentrations, increased ink volatility and reduced coordination of the precursor solvents accelerates nucleation at the top-surface, induced by the gas-jet. This results in the formation of a solidified "crust" at the film surface and the formation of voids throughout the bulk of the film. The pinholes observed between grains in the 0:10 films, and the interfacial voids within films prepared from solutions at higher THF concentrations account for the reduced device efficiency compared to those prepared from the "champion" 1:9 composition. This finding is evidenced by a reduction in all device metrics.

To further probe the formation of functional films from the 1:9 THF:2-ME solvent system, we performed in situ grazing incidence wide-angle X-ray scattering (GIWAXS) measurements on solutions deposited via blade-coating (see schematic shown in Figure S8 (Supporting Information), full methods are available in the Experimental Section). To mirror the spin-coating protocol, films were continuously gas-quenched after deposition, with coating performed in an N$_2$ atmosphere. We observed that the as-deposited film exhibits amorphous scattering (see Figure S9a, Supporting Information), which is typical for a disordered solvate phase. Immediately after gas-quenching, however, we observed the presence of two distinct intermediate phases during the crystallization process. The first is characterized by an oriented intermediate phase (**1**) with characteristic reflections at $Q = 0.42$ and 0.84 Å^{-1} ($2\theta = 5.9°$ and $11.9°$), see **Figure 4**a). This rapidly ($\approx$1 s) evolved into a second highly textured phase (**2**, see Figure 4b) with a broad peak at $Q = 0.59$ Å^{-1} ($2\theta = 8.2°$), which gradually reduced in intensity over the course of the measurement (see Figure S9b,c,

Supporting Information). The appearance of phase **2** is concurrent with the emergence of peaks corresponding to tetragonal MAPbI$_3$[61] which grow as a function of time (see Figure 4c). Azimuthal integrations of the scattering pattern of each phase are given in Figure S10 (Supporting Information). Here, we evidence peaks which possibly correspond to a 2H polytype phase that has been theoretically proposed for MAPbI$_3$,[63] but has not been observed when simply spin coating such films. We suspect this observation may result somehow from the fact that the GIWAXS blade coating studies explored a relatively thicker film, with the nature of the coating procedure perhaps also being significant. Importantly, neither intermediate phase **1** nor phase **2** was detected in the XRD patterns of the spin-fabricated films (see Figure 3a). This result indicates that the intermediate phases that form during the initial crystallization process are readily converted to a perovskite phase at room temperature, most likely due to the weak coordinating ability of the two solvents. This is not the case for MAPbI$_3$ intermediate phases formed using typical solvents such as DMF and DMSO, which are generally stable at room temperature.[64,65]

We have also explored thermally annealing such blade-coated films while recording GIWAXS spectra as shown in Figure S11 (Supporting Information). Here, we find that intermediate phase **2** was completely removed at around 70 °C, and that heating the film above 50 °C improved the crystallinity of MAPbI$_3$. We speculate that this may explain the observed performance enhancement upon light-soaking of annealing free devices. Indeed, we suspect that the in operando heating of annealing-free devices may improve the crystallinity of devices during testing.

To further evaluate the utility of our annealing-free approach, we compare our device performance to that of conventionally annealed devices. The same p-i-n architecture was used as in Figure 1b, but the perovskite film (fabricated from the 1:9 THF:2-ME composition) was annealed at 100 °C for 10 min. For clarity, this process versus an "annealing-free MAPbI$_3$" process is schematically illustrated in Figure S12a,b (Supporting Information). Boxplots of the annealing-free MAPbI$_3$ device performance metrics versus those of the annealed MAPbI$_3$ devices are presented in Figure S13 (Supporting Information). We find that although the median device PCE is improved from 14.9% to 16.0% upon annealing the perovskite, this median value falls within the interquartile range (IQR) of the annealing-free devices. For this reason, we conclude that there is only a slight statistical improvement in device performance upon annealing. If we compare the EQE spectra of the champion annealing-free MAPbI$_3$ device against that of the best-performing annealed-MAPbI$_3$ device (see **Figure 5**a), we observe only a small increase in the EQE of the annealed device over the wavelength range 600–800 nm. We attribute this increase upon annealing to improved charge carrier collection which in turn results from an increase in grain size and morphology during the annealing treatment.[66,67] This can be evidenced by the XRD patterns and SEM images presented in Figure 5b–d, respectively. The full SEM images are presented in Figure S14 (Supporting Information). Here, a significant enlargement of the perovskite grain size and an enhancement in the crystallinity of the perovskite film upon annealing can be clearly seen. We also observe a reduced splitting of the tetragonal (220)/ (004) diffraction peaks
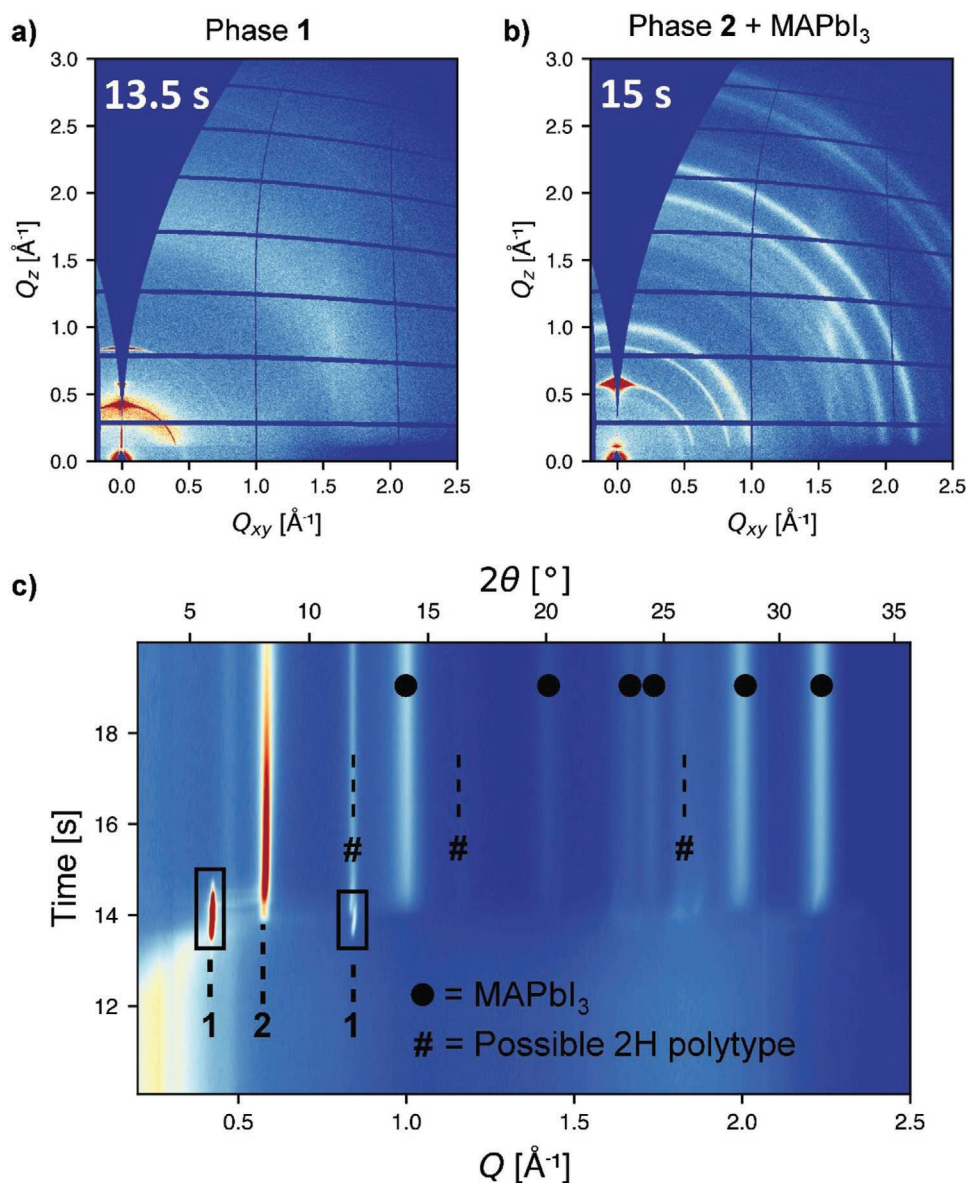
**ADVANCED
SCIENCE NEWS**

www.advancedsciencenews.com

**ADVANCED
ENERGY
MATERIALS**

www.advenergymat.de

Figure 4. Grazing incidence wide-angle X-ray scattering (GIWAXS) of a) phase **1** at 13.5 s and b) phase **2** and MAPbI$_3$ at 15 s. c) 1D integrated in situ GIWAXS highlighting the 10–20 s time period following blade coating. At around 13 s, the solvate phase shifts to higher angles as solvent is removed, followed by the crystallization of phase **1**, which rapidly converts to phase **2** at ≈14 s, which rapidly reduces in intensity over a period of ≈5 s, with MAPbI$_3$ then becoming the dominant material phase.

at 28.3° and 28.6° 2θ, which may indicate a change in the unit cell geometry upon annealing.

We therefore ascribe the overall increase in device performance upon annealing to an increase in J_{SC} arising from enhanced charge carrier extraction, with both the FF and V_{OC} of annealed devices remaining statistically similar to that of devices containing an annealing-free active layer (see Figure S9, Supporting Information). Here, we note that interfacial voids are observed in the cross-sectional SEM image of the annealed perovskite film which can be seen in Figure S15 (Supporting Information). Such voids presumably arise due to strain effects during the crystalline growth process and may limit the overall PCE of the annealed devices. The corresponding J–V curve, EQE with integrated current density, and SPO of the champion

annealed MAPbI$_3$ device are plotted in Figure S16a–c (Supporting Information). Here, the champion stabilized PCE of 18.4% for this annealed device compares extremely favorably to the champion anneal-free MAPbI$_3$ device (18.0% stabilized). We conclude, therefore, that the 1:9 THF:2-ME solvent system facilitates the fabrication of annealing-free MAPbI$_3$ films with excellent crystalline and optoelectronic properties.

2.2. Stability of Ink and Devices

To examine the stability of our annealing-free devices, we have periodically recorded J–V characteristics of devices stored in a glovebox, under N$_2$ and in the dark. All J–V measurements

**ADVANCED
SCIENCE NEWS**

www.advancedsciencenews.com
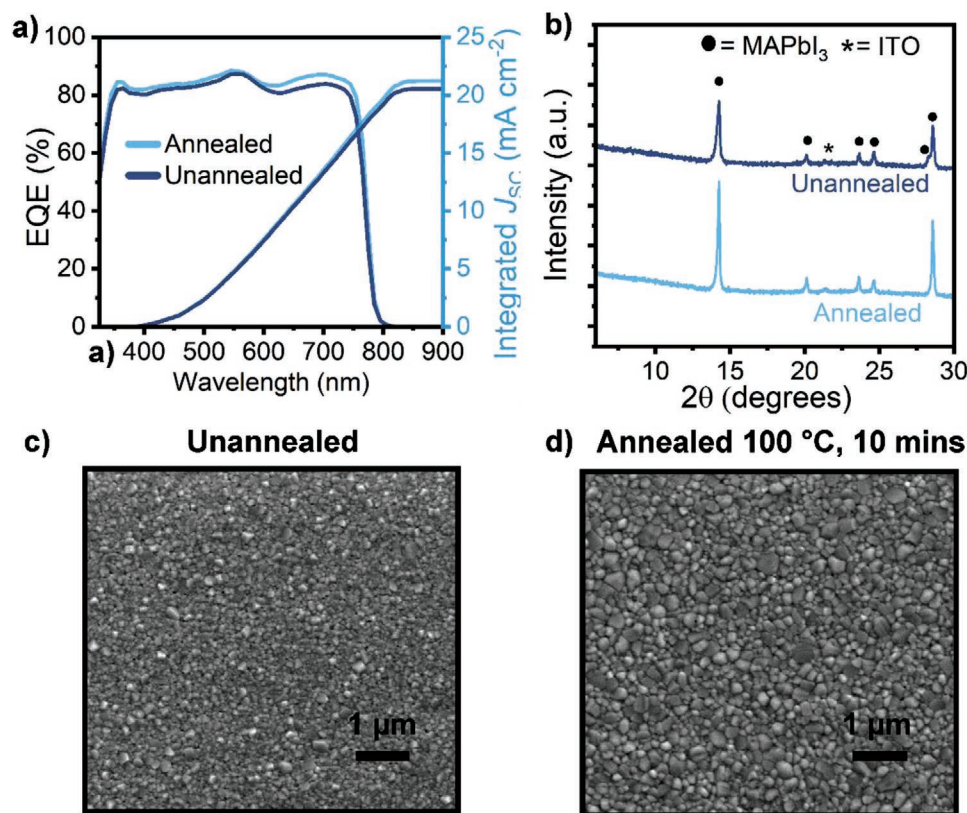
**ADVANCED
ENERGY
MATERIALS**

www.advenergymat.de

Figure 5. a) External quantum efficiencies of cells with an unannealed or annealed (100 °C for 10 min) active layer. b) X-ray diffraction (XRD) patterns of annealed and unannealed perovskite film cast from the 1:9 precursor ink. Scanning electron microscope (SEM) images of the surface of the perovskite absorber layer fabricated from a 1:9 tetrahydrofuran (THF):2-methoxyethanol (2-ME) precursor ink c) without annealing and d) with an annealing treatment (100 °C, 10 min).

were conducted in air. **Figure 6**a shows the mean with whiskers indicating the minimum/maximum of device PCEs for 16 cells (including both forward and reverse J–V sweep) as a function of storage time. We observe a slight increase in the mean PCE of the devices as they age. Indeed, after 15 days, we observe a 1% absolute increase in the mean value of device PCE. This spontaneous enhancement of the performance of the dark-stored PCE has previously been attributed to a reduction in trap-assisted nonradiative recombination, perhaps caused by a reduction in film strain.[68] We have applied a linear regression model ($y = 15.23 - 0.007 \times x$) to determine whether the shelf-age of the devices can be used to predict the device performance upon retesting. The model results indicate that shelf-age of the device was not a significant predictor of device performance,

with the slope coefficient not significantly different from zero ($F(1, 156)$, $p = 0.177$, $R^2 = 0.012$). This 9-week shelf-life of devices indicates a promising level of intrinsic stability. From this, we infer that annealing-free films are not likely to contain residual, trapped solvent which would be expected to induce intrinsic instability by slowly corroding or otherwise degrading the perovskite thin films.

It is important that any perovskite precursor inks should demonstrate a high degree of intrinsic stability, as this will make them compatible with a practical manufacturing process. We have previously demonstrated that storing precursor inks at low-temperature can extend their shelf life, however solvent choice is known to have a significant impact on solution stability.[69] We therefore investigated the shelf-life of the
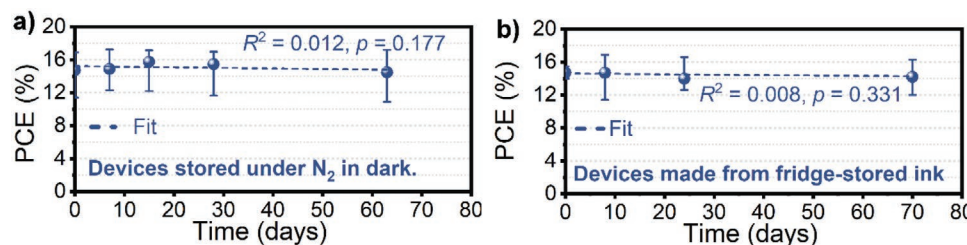

Figure 6. a) The power conversion efficiency (PCE) of devices containing an annealing-free perovskite absorber layer stored in a glovebox in the dark and retested periodically over 2 months. b) The PCE of cells periodically fabricated from the 1:9 ink stored in the fridge.

**ADVANCED
SCIENCE NEWS**

www.advancedsciencenews.com

**ADVANCED
ENERGY
MATERIALS**

www.advenergymat.de

1:9 THF:2-ME MAPbI$_3$ precursor ink when stored at low temperature (≈4 °C). To do this, devices were periodically fabricated from a single batch of a fridge-stored ink. Figure 6b shows the resulting device PCEs over a period of 10 weeks ink storage-time, plotted as the mean ± minimum/maximum device PCE for both the forward and reverse J–V sweep of at least 16 cells per time point. Again, a linear regression was used to test whether the ink age (storage time) significantly predicted the resultant device PCE. The fitted regression model was ($y = 14.5 − 0.005 \times x$) and the slope was again not significantly different from zero ($F_{(1, 118)}$, $p = 0.331$, $R^2 = 0.008$). We therefore found no statistical difference in the device PCEs over this storage timeframe. This negligible deterioration demonstrates excellent solution stability for the THF:2-ME mixture containing MAPbI$_3$ precursor materials.

Previous work has shown that methylamine—either introduced directly as a precursor solvent[59] or formed via degradation of methylammonium—accelerates the degradation of formamidinium (FA) containing perovskite precursor inks. In those systems, the methylamine participates in a series of addition–elimination reactions, forming further secondary reaction products which result in the formation of nonperovskite polytype phases in the resultant perovskite thin film.[70] Here, we avoid the use of methylamine as a solvent. We therefore speculate that a THF:2-ME binary solvent system is also likely to have a high degree of stability when used with FA-based perovskite precursors.

2.3. Fully Annealing-Free Fabrication of Perovskite Solar Cells

To make a fully annealing-free PSC, the charge transporting layers must also be fabricated without annealing steps in a high-speed R2R process. To date, there are very few demonstrations of annealing-free perovskite layers combined with annealing-free transport layers. Many reports use ZnO, TiO$_2$, or SnO$_2$ ETLs which require high temperature sintering steps. UV-ozone treatments can be used to replace the annealing of SnO$_2$,[20] but such treatments can take upwards of 30 min, thus eliminating any benefit to manufacturing throughput. Notably, Jiang et al. fabricated an Nb$_2$O$_5$-TiO$_2$ ETL at room temperature but this required the application of a time-consuming 15-min UV-ozone treatment prior to deposition of the perovskite.[19] Such methods also required the use of antisolvent treatments to fabricate the annealing-free perovskite layer. The HTL poly(3,4-ethylenedioxythiophene) polystyrene sulfonate (PEDOT:PSS) can be deposited without any requirement for thermal annealing, however, it is known to be hygroscopic and typically needs annealing treatments to remove residual water to prevent device instability.[71] Wang et al. successfully created fully annealing-free PSCs having efficiencies of up to 16.40% using a room-temperature dried PEDOT:PSS HTL.[72] We note, however, that the 60-min water vapor annealing treatment used is incompatible with a high speed R2R process. In 2015, Su et al. developed HTL-free, annealing-free PSCs by thermal evaporation, demonstrating PCEs of up to 8.37%.[12] In 2016, Zhao et al. thermally deposited fully annealing-free PSCs having efficiencies of up to 15.7% (14.6% stabilized).[13]

To create fully annealing-free PSCs, we have investigated the performance of devices based on the HTL MeO-2PACz without the application of a heating treatment. The chemical structure of MeO-2PACz is included in Figure S17 (Supporting Information). Although annealing of SAMs after deposition is a ubiquitous process—and is expected to strengthen the bonding between the SAM and the underlying substrate[73]—we demonstrate that sufficient binding occurs spontaneously during deposition of MeO-2PACz to create efficient PSCs without the necessity of annealing. In our experiments, we spin coat the MeO-2PACz and 1:9 MAPbI$_3$ precursor as described above, without using an annealing step for either layer (see Figure S12c, Supporting Information, for schematic). Again, devices were completed with a thermally evaporated C$_{60}$/BCP/Ag cathode to realize fully annealing-free cells. In **Figure 7**a, we show a statistical summary of device performance comparing such fully annealing-free devices against devices with an annealed MeO-2PACz HTL and an unannealed MAPbI$_3$ active layer. Notably, we find very little statistically significant difference between such devices. For completeness, **Table 1** summarizes the performance of devices made from the three combinations of annealed/unannealed MeO-2PACz and MAPbI$_3$ layers that are discussed above.

To further explore the quality of the unannealed MeO-2PACz layer, we conducted X-ray photoelectron spectroscopy (XPS) analysis to compare the surface chemistry of annealed and unannealed MeO-2PACz layers (Figure 7b,c). The MeO-2PACz phosphonic acid group contains three oxygen atoms capable of covalently binding to ITO surface oxides : two hydroxyl groups and a phosphoryl moiety. A large number of different binding modes are available, either through hydrogen bonding interactions with surface hydroxyl groups or neighboring SAMs, or via condensation reactions which can form up to three P–O–M bonds (where M in the metal–oxide substrate) between each SAM and the surface.[74] The strength of the coordination between the SAM and the surface dictates the robustness of the layer. Such condensation reactions—particularly those increasing the denticity of the binding mode—are conventionally thought to occur during annealing treatments after the deposition of the SAM.

To investigate whether a change in the denticity of the binding modes (i.e., a shift in the chemical environment of the P or O centers) upon annealing could be detected, we recorded high-resolution O 1s and P 2p spectra in order to investigate the binding of the phosphonic acid tail group to the ITO substrate, as demonstrated previously.[75] While we find that there is a clear difference in the O 1s spectra between the bare ITO-coated glass substrate and the MeO-2PACz coated samples—as expected due to the additional O-containing groups within the MeO-2PACz structure—there is no difference in either the O 1s or P 2p environments of the MeO-2PACz as a consequence of the annealing treatment. Similarly, we find no significant difference in the contact angle of a water droplet on the surface of the annealed versus unannealed MeO-2PACz (54.6 ± 3.1° versus 53.0 ± 1.7°, respectively, see Figure 7d). We suspect that such small changes may arise from a change in the surface coverage of the MeO-2PACz.

We postulate that the binding energy for the condensation reaction between the phosphonic acid tail group and the ITO surface is sufficiently low to occur at room temperature. This is
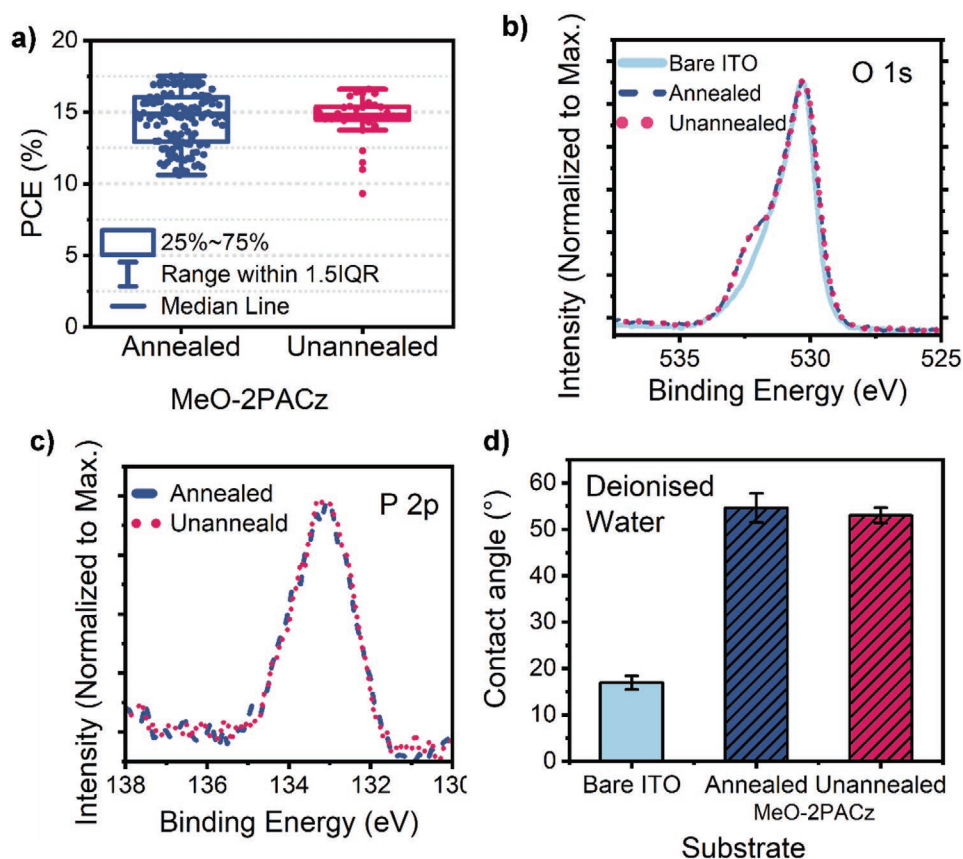
ADVANCED
SCIENCE NEWS
www.advancedsciencenews.com

ADVANCED
ENERGY
MATERIALS
www.advenergymat.de

Figure 7. a) A boxplot comparing the power conversion efficiency (PCE) of devices containing an annealing-free perovskite absorber layer with an annealed MeO-2PACz hole-transporting layer (HTL) (blue) and an unannealed MeO-2PACz HTL (purple). High-resolution X-ray photoelectron spectroscopy (XPS) spectra of the b) O 1s and c) P 2p regions of bare indium tin-oxide (ITO) coated glass (light blue, solid), ITO with spin-coated and annealed MeO-2PACz (dark blue, dashed), and ITO with spin-coated, unannealed MeO-2PACz (purple, dotted). d) The contact angle of a water droplet on bare ITO-coated glass (light blue), an annealed MeO-2PACz film (dark blue), and an unannealed MeO-2PACz film (green).

in agreement with previous studies in which phosphonic acid-containing SAMs deposited at room-temperature were found to remain on the surface after "extensive rinsing and sonication," indicating strong chemisorption between the SAM and the surface at room temperature.[76]

We therefore find that annealing the deposited MeO-2PACz layer is not necessary for the formation of a high-quality HTL. Using this approach, we have fabricated fully annealing-free PSCs with a champion stabilized efficiency of 17.1% (Figure S18a–c, Supporting Information), with little statistically significant variation in comparison to PSCs with an annealed MeO-2PACz

HTL (anneal-free MAPbI₃). Again, the $J_{SC\text{-}JV}$ matches well with the calculated $J_{SC\text{-}EQE}$.

To our knowledge, this represents the highest performance demonstrated for a PSC fabricated without any annealing treatments in a fully R2R compatible manner. We compare our work to other fully annealing-free approaches as discussed above in **Figure 8**.

Finally, we recently reported the use of gas-quenching to fabricate spray-coated MAPbI₃ perovskite films, and the spray deposition of MeO-2PACz as an HTL.[39] We believe that the binary solvent precursor ink explored here will be a

Table 1. A summary of perovskite solar cell (PSC) performance metrics (including both forward and reverse J–V sweeps) for all devices presented in this work.

MeO-2PACz	MAPbI₃	J_{SC} [mA cm⁻²]	V_{OC} [V]	FF [%]	PCE [%]	n_{cells}
🔥	🔥	(21.1 ± 0.8) **22.4**	(1.06 ± 0.03) **1.08**	(75.3 ± 6.2) **80.3**	(15.9 ± 1.7) **18.0**	24
🔥	❄	(19.4 ± 1.2) **21.2**	(1.05 ± 0.05) **1.11**	(72.5 ± 4.7) **78.0**	(14.9 ± 1.9) **17.5**	62
❄	❄	(19.2 ± 0.5) **20.4**	(1.08 ± 0.05) **1.09**	(72.4 ± 5.6) **76.6**	(14.8 ± 1.6) **16.6**	16

Bold font data represents the champion performance metric, with median ± standard deviation values presented in parentheses. 🔥 is annealed, ❄ is unannealed.
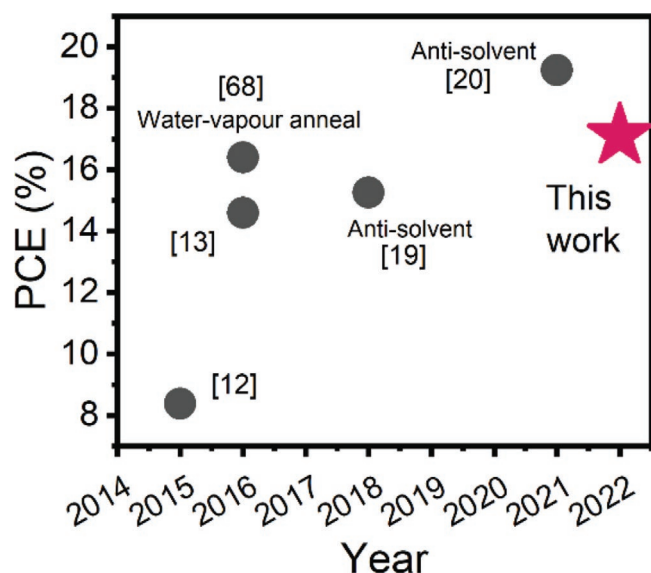
Figure 8. A comparison of reported device power conversion efficiencies (PCEs) in the literature for fully annealing-free fabrication of perovskite solar cells. The annotations indicate the use of processing steps with limited scalability.

promising candidate to spray coat the perovskite without the necessity of annealing. Previously, our attempts to spray coat ACN-based precursors have been unsuccessful due to the higher vapor pressure of ACN (88.8 mm Hg at 25 °C) leading to the premature evaporation of the precursor droplets before reaching the substrate surface. Here, the 1:9 THF:2-ME ink is expected to have a sufficiently low vapor pressure to allow it to be spray-deposited and undergo room-temperature removal of the casting solvents. We believe that spray coating fully annealing free devices would have direct commercial relevance as a route to extremely high-throughput R2R fabrication of PSCs.

3. Conclusions

We have developed a novel two-component solvent system combining THF and 2-ME to fabricate crystalline MAPbI$_3$ thin-films at room temperature following simple gas-jet-induced evaporation of the casting solvents. Without the THF, the pure 2-ME precursor inks form discontinuous perovskite films characterized by a large number of pinholes. By adding THF to the 2-ME, we are able to modify the vapor pressure of the binary system. This results in a lower degree of solvent coordination to the lead centers, a finding in agreement with theoretical predictions. The THF component therefore accelerates the solvent removal during the "gas-quench." This results in a greater degree of nucleation with a dense and uniform film created having a smaller average grain size with respect to the pure 2-ME composition. We find, however, that if too much THF is incorporated, a rapid, top-down evaporation process occurs, resulting in a solidified top layer with a series of voids formed throughout the underlying film. At the optimized composition of 10 vol% THF, however, we tune the evaporation rate to obtain

uniform, pinhole-free perovskite films. Using this approach, we fabricate p-i-n PSCs incorporating an annealing-free perovskite layer and demonstrate stabilized device efficiencies up to 18.0%. These PCEs are completely comparable to those demonstrated in devices incorporating annealed perovskite films, underpinning the practicality of our approach.

Finally, we removed the annealing step typically employed during the deposition of SAM molecules as HTLs. We observed only a small loss in device performance when foregoing the MeO-2PACz annealing process. By combining an anneal-free MeO-2PACz film with an anneal-free 1:9 THF:2-ME perovskite layer, we created devices having stabilized PCEs of up to 17.1%. This is the highest device performance demonstrated so far for a fully annealing-free PSC that is completely compatible with a high-speed, high-volume R2R process.

In summary this work demonstrates a facile route to fabricate efficient PSCs without any lengthy annealing steps to process either the charge transporting layers or the perovskite itself. The binary solvent precursor ink demonstrates good storage stability and is identified as an ideal candidate for rapid spray deposition. These results therefore represent a promising route for low-cost, high-speed, and high-volume industrial production of PSCs.

4. Experimental Section

Materials: All materials were used as received without any further purification. MeO-2PACz (>98%) and PbI$_2$ (>99.99% trace metals basis) were purchased from Tokyo Chemical Industry. Methylammonium iodide (MAI, >99.9%) and 20 ×15 mm prepatterned ITO (≈20 Ω □$^{-1}$) substrates were purchased from Ossila. All solvents and remaining materials including C$_{60}$ (sublimed, 99.99%) and bathocuproine (BCP, sublimed, 99.99%) were purchased from Sigma–Aldrich unless otherwise stated. ITO substrates were cleaned by sequential sonication in diluted Helmanex solution, boiling deionized water, acetone, and iso-propanol (IPA). After drying under flow of N$_2$, the substrates were UV ozone treated for 15 min immediately prior to device processing.

Device Fabrication: A stock solution of the MeO-2PACz (1 mmol in ethanol) was prepared and stored under N$_2$, with a small amount decanted for use as necessary. We have so far found this stock solution to be stable (no difference in resulting device performance) over a period of 18 months. An amount of 60 µL of MeO-2PACz solution was statically spin-coated onto the substrate for 30 s at 3000 rpm in a N$_2$ filled glovebox. Where the MeO-2PACz was annealed, the as-spun films were transferred to a hotplate at 100 °C for 10 min. No subsequent rinsing steps were applied.

A MAPbI$_3$ precursor ink (0.5 м) was prepared in different compositions of THF:2-ME. Stoichiometric quantities of MAI and PbI$_2$ (i.e., 79.5 and 230.5 mg mL^{-1}, respectively) were dissolved in the appropriate ratio of the two solvents and dissolved by stirring overnight. The best-performing binary composition investigated here was based on a 1:9 ratio of THF:2-ME. The precursor inks were spin-coated at 800 rpm s^{-1} for 5 s, then 4000 rpm for 35 s. At 6 s into the spin-cycle, a "gas-quench" was employed wherein an N$_2$ flow of ≈20 psi was directed at the spinning substrate, immediately inducing a color change from yellow to dark brown.

The C$_{60}$/BCP ETL was thermally evaporated (Angstrom Engineering) at a chamber base pressure of at least 2.4 × 10^{-6} mbar from alumina crucible sources (RADAK, Luxel Corp.) at a constant rate of 0.1 Å s^{-1}. Silver pellets (Lesker) were deposited from a resistive boat source at a ramped rate of 0.1–1.0 Å s^{-1} through a shadow mask to form the Ag back-electrode. Devices were then encapsulated using an epoxy pen (Bluefixx Blue LED Repair Pen, Combined Precision Components) and glass encapsulation coverslips (Ossila).

Device Characterization: Current–voltage (*J*–*V*) measurements were recorded under ambient conditions using a Newport 92251A-1000 solar simulator. No preconditioning of devices was carried out. Prior to testing, the Air Mass 1.5 (AM1.5) spectrum was adjusted to 100 mW cm^{-2} at the substrate holder location using a National Renewable Energy Laboratory (NREL) certified silicon reference cell. The active measurement area was defined using metal aperture masks with a calibrated area of 2.5 mm^2. A Keithley 237 source-measure unit swept devices between −0.1 and 1.2 V at 50 mV s^{-1}. SPO measurements were performed by holding the device at a bias defined by the average voltage at maximum power (V_{mpp}) determined from the forward and reverse sweeps.

EQE measurements were recorded over a 325–900 nm range using a Newport QuantX-300 Quantum Efficiency Measurement System. The system was equipped with a 100 W Xenon arc lamp focused through an Oriel Monochromator (CS130B) and chopped at 25 Hz.

X-ray diffraction (XRD) patterns were recorded at room temperature using a PANalytical X'Pert^3 diffractometer equipped with a Cu line focus X-ray tube run at 45 kV with a tube current of 40 mA. The 1D detector collected data in Bragg–Brentano geometry.

SEM images were recorded using an FEI Nova Nano450 SEM operating at a beam energy of 1.5 kV at a working distance of 4–5 mm, with an in-lens detector used to collect backscattered electrons.

AFM (Veeco Dimension 3100) images were collected in Intermittent Contact (Tapping) Mode with a NuNano Scout 350 cantilever (nominal spring constant 42 N m^{-1}, resonant frequency 350 kHz). Each sample was scanned over a 5 × 5 μm area with a resolution of 512 × 512 pixels.

Film thickness measurements were collected using a Bruker Dektak XT system. A razor blade was used to scratch the perovskite thin films prepared as described above. The profilometer tip (12.5 μm diameter) was scanned 1000 μm across this "scratch" in the film surface at a stylus force of 3 mg. Vison64 software (Bruker) was used to level the 1D line scan and extract a step height from the film surface to the bottom of the scratched valley.

In situ GIWAXS data was acquired at the I07 beamline at Diamond Light Source. Solutions were deposited using an in situ blade coater contained in an N$_2$ environment incorporating a syringe driver, coating surface, motorized blade, integrated hotplate, and an N$_2$ outlet directed at the sample surface for gas-quenching. Prior to data acquisition, solutions were deposited onto cleaned glass substrates with a shim height of 40 μm and a coating speed of 9 mm s^{-1}. Monochromatic X-rays with an energy of 10 keV were incident on the samples at a grazing incidence angle of 1°, with scattering collected by a Pilatus 2 M (DECTRIS) hybrid photon-counting detector at a distance of 365 mm, with the geometry calibrated using LaB6. 2D detector images were acquired every 0.1 s. Data reduction was performed using scripts based on the pyFAI and pygix libraries.[77]

For XPS measurements, the ITO-coated glass substrates were mounted onto the sample holder with double-sided carbon tape, and then copper alloy bars were screwed into the sample holder in such a way that they overlapped slightly the top and bottom edges of each sample in order to ensure the treated surface was not electrically isolated. Charge neutralization was also used to prevent surface charge build-up. Analysis was carried out using a Kratos Supra instrument with a monochromated aluminum source, with two analysis points recorded per sample over an area of 700 by 300 μm. Survey scans were collected between 1200 to 0 eV binding energy, at 160 eV pass energy, 1 eV intervals, and 300 s per sweep with one sweep being collected. High-resolution O 1s, C 1s, In 3d, N 1s, and P 2p XPS spectra were also collected at 20 eV pass energy and 0.1 eV intervals for each analysis point over an appropriate energy range, with one 300 s sweep used to record all spectra except N 1s and P 2p for which two sweeps were collected. The data collected was calibrated in intensity using a transmission function characteristic of the instrument to make the values instrument independent. The data was then quantified using theoretical Schofield relative sensitivity factors modified to account for instrument geometry, variation in penetration depth with energy, and the angular distribution of the photoelectrons. The binding energy scale was calibrated for all samples by fixing In 3d5/2 at 444.57 eV. This In 3d5/2 value puts the main C 1s peak for the ITO samples at 285.0 eV, consistent with the assumption that it results from carbonaceous contamination.

Contact angle measurements of droplets on thin-films were performed using a contact angle goniometer (Ossila). A small droplet of water was deposited onto the substrate surface and recorded at 20 fps. The Ossila contact angle software was then used to extract the angle between the droplet and the sample surface at the point of initial contact.

UV–Visible transmission measurements were recorded using a Fluoromax-4 fluorometer (Horiba), with corresponding absorbance values calculated according to the logarithmic relationship $A = -\log_{10} T$. Precursor inks were diluted to 0.05 M to prevent saturation of the detector and referenced to the empty quartz cuvette used for measurements. UV–Vis measurements for the precursor inks were recorded over the spectral range 250–500 nm.

Optical microscope images were recorded using a Nikon Eclipse ME600 microscope at 50× magnification.

Supporting Information

Supporting Information is available from the Wiley Online Library or from the author.

Conflict of Interest

D.G.L. is co-founder and Chairman of materials science company Ossila that retails products for research and development of optoelectronic devices, including perovskite solar cells. C.J.W. is an employee of Power Roll Ltd. who are developing solar cell devices based on perovskites. H.J. Snaith is co-founder and CSO of Oxford PV Ltd.

Data Availability Statement

The data that support the findings of this study are available from the corresponding author upon reasonable request.

Keywords

[1] NREL, https://www.nrel.gov/pv/cell-efficiency.html, **2022**.

[2] Y. Deng, E. Peng, Y. Shao, Z. Xiao, Q. Dong, J. Huang, *Energy Environ. Sci.* **2015**, *8*, 1544.

[3] K. Hwang, Y.-S. S. Jung, Y.-J. J. Heo, F. H. Scholes, S. E. Watkins, J. Subbiah, D. J. Jones, D.-Y. Y. Kim, D. Vak, *Adv. Mater.* **2015**, *27*, 1241.

[4] A. T. Barrows, A. J. Pearson, C. K. Kwak, A. D. F. Dunbar, A. R. Buckley, D. G. Lidzey, *Energy Environ. Sci.* **2014**, *7*, 2944.

[5] N. Rolston, W. J. Scheideler, A. C. Flick, J. P. Chen, H. Elmaraghi, A. Sleugh, O. Zhao, M. Woodhouse, R. H. Dauskardt, *Joule* **2020**, *4*, 2675.

[6] F. Hilt, M. Q. Hovish, N. Rolston, K. Brü, C. J. Tassone, R. H. Dauskardt, *Energy Environ. Sci.* **2018**, *11*, 2102.

[7] K. Bruening, B. Dou, J. Simonaitis, Y. Y. Lin, M. F. A. M. van Hest, C. J. Tassone, *Joule* **2018**, *2*, 2464.

[8] Z. Song, C. L. McElvany, A. B. Phillips, I. Celik, P. W. Krantz, S. C. Watthage, G. K. Liyanage, D. Apul, M. J. Heben, *Energy Environ. Sci.* **2017**, *10*, 1297.

[9] J. Panidi, D. G. Georgiadou, T. Schoetz, T. Prodromakis, *Adv. Funct. Mater.* **2022**, *32*, 2200694.

[10] C. Polyzoidis, K. Rogdakis, E. Kymakis, *Adv. Energy Mater.* **2021**, *11*, 2101854.

[11] I. Mathews, S. Sofia, E. Ma, J. Jean, H. S. Laine, S. C. Siah, T. Buonassisi, I. M. Peters, *Joule* **2020**, *4*, 822.

[12] Z. Su, F. Hou, F. Jin, L. Wang, Y. Li, J. Zhu, B. Chu, W. Li, *Org. Electron.* **2015**, *26*, 104.

[13] D. Zhao, W. Ke, C. R. Grice, A. J. Cimaroli, X. Tan, M. Yang, R. W. Collins, H. Zhang, K. Zhu, Y. Yan, *Nano Energy* **2016**, *19*, 88.

[14] F. Zhou, H. Liu, X. Wang, W. Shen, *Adv. Funct. Mater.* **2017**, *27*, 1606156.

[15] X. Zheng, B. Chen, C. Wu, S. Priya, *Nano Energy* **2015**, *17*, 269.

[16] M. Yin, F. Xie, H. Chen, X. Yang, F. Ye, E. Bi, Y. Wu, M. Cai, L. Han, *J. Mater. Chem. A* **2016**, *4*, 8548.

[17] X. Fang, Y. Wu, Y. Lu, Y. Sun, S. Zhang, J. Zhang, W. Zhang, N. Yuan, J. Ding, *J. Mater. Chem. C* **2017**, *5*, 842.

[18] M. M. Byranvand, S. Song, L. Pyeon, G. Kang, G.-Y. Lee, T. Park, *Nano Energy* **2017**, *34*, 181.

[19] J. Jiang, S. Wang, X. Jia, X. Fang, S. Zhang, J. Zhang, W. Liu, J. Ding, N. Yuan, *RSC Adv.* **2018**, *8*, 12823.

[20] H. Dong, S. Pang, F. He, H. Yang, W. Zhu, D. Chen, H. Xi, J. Zhang, Y. Hao, C. Zhang, *Sol. RRL* **2021**, *5*, 2100097.

[21] C. Dong, J. Chen, C.-H. Chen, Y.-R. Shi, W.-F. Yang, K.-L. Wang, Z.-K. Wang, L.-S. Liao, *Nano Energy* **2022**, *94*, 106866.

[22] M.-R. Ahmadian-Yazdi, M. Eslamian, *Mater. Today Commun.* **2018**, *14*, 151.

[23] X. Zhang, F. Zabihi, H. Xiong, M. Eslamian, C. Hou, M. Zhu, H. Wang, Q. Zhang, *Chem. Eng. J.* **2020**, *394*, 124887.

[24] H. Xiong, F. Zabihi, H. Wang, Q. Zhang, M. Eslamian, *Nanoscale* **2018**, *10*, 8526.

[25] B. Yang, O. Dyck, J. Poplawsky, J. Keum, S. Das, A. Puretzky, T. Aytug, P. C. Joshi, C. M. Rouleau, G. Duscher, D. B. Geohegan, K. Xiao, *Angew. Chem., Int. Ed.* **2015**, *54*, 14862.

[26] A. Dubey, N. Kantack, N. Adhikari, K. M. Reza, S. Venkatesan, M. Kumar, D. Khatiwada, S. Darling, Q. Qiao, *J. Mater. Chem. A* **2016**, *4*, 10231.

[27] C. Wu, K. Wang, J. Li, Z. Liang, J. Li, W. Li, L. Zhao, B. Chi, S. Wang, *Matter* **2021**, *4*, 775.

[28] G. S. Shin, W.-G. Choi, S. Na, S. O. Ryu, T. Moon, *Electron. Mater. Lett.* **2017**, *13*, 72.

[29] Z. Wang, X. Zhu, J. Feng, C. Wang, C. Zhang, X. Ren, S. Priya, S. (Frank) Liu, D. Yang, *Adv. Sci.* **2021**, *8*, 2002860.

[30] K. Wang, C. Wu, Y. Hou, D. Yang, T. Ye, J. Yoon, M. Sanghadasa, S. Priya, *Energy Environ. Sci.* **2020**, *13*, 3412.

[31] Q. Liu, Y. Zhao, Y. Ma, X. Sun, W. Ge, Z. Fang, H. Bai, Q. Tian, B. Fan, T. Zhang, *J. Mater. Chem. A* **2019**, *7*, 18275.

[32] G. Wang, L. Liao, L. Chen, C. Xu, Y. Yao, D. Liu, P. Li, J. Deng, Q. Song, *Org. Electron.* **2020**, *86*, 105918.

[33] K. H. Hendriks, J. J. van Franeker, B. J. Bruijnaers, J. A. Anta, M. M. Wienk, R. A. J. Janssen, *J. Mater. Chem. A* **2017**, *5*, 2346.

[34] Y. Deng, C. H. Van Brackle, X. Dai, J. Zhao, B. Chen, J. Huang, *Sci. Adv.* **2019**, *5*, eaax7537.

[35] S. Chen, X. Dai, S. Xu, H. Jiao, L. Zhao, J. Huang, *Science* **2021**, *373*, 902.

[36] D.-K. Lee, D.-N. Jeong, T. K. Ahn, N.-G. Park, *ACS Energy Lett.* **2019**, *4*, 2393.

[37] J. W. Yoo, J. Jang, U. Kim, Y. Lee, S.-G. Ji, E. Noh, S. Hong, M. Choi, S. Il Seok, *Joule* **2021**, *5*, 2420.

[38] J. Li, J. Dagar, O. Shargaieva, M. A. Flatken, H. Köbler, M. Fenske, C. Schultz, B. Stegemann, J. Just, D. M. Többens, A. Abate, R. Munir, E. Unger, *Adv. Energy Mater.* **2021**, *11*, 2003460.

[39] E. J. Cassella, E. L. K. Spooner, T. Thornber, M. E. O'Kane, T. E. Catley, J. E. Bishop, J. A. Smith, O. S. Game, D. G. Lidzey, *Adv. Sci.* **2022**, *9*, 2104848.

[40] A. Al-Ashouri, A. Magomedov, M. Roß, M. Jošt, M. Talaikis, G. Chistiakova, T. Bertram, J. A. Márquez, E. Köhnen, E. Kasparavičius, S. Levcenco, L. Gil-Escrig, C. J. Hages, R. Schlatmann, B. Rech, T. Malinauskas, T. Unold, C. A. Kaufmann, L. Korte, G. Niaura, V. Getautis, S. Albrecht, *Energy Environ. Sci.* **2019**, *12*, 3356.

[41] A. Al-Ashouri, E. Köhnen, B. Li, A. Magomedov, H. Hempel, P. Caprioglio, J. A. Márquez, A. B. Morales Vilches, E. Kasparavicius, J. A. Smith, N. Phung, D. Menzel, M. Grischek, L. Kegelmann, D. Skroblin, C. Gollwitzer, T. Malinauskas, M. Jošt, G. Matič, B. Rech, R. Schlatmann, M. Topič, L. Korte, A. Abate, B. Stannowski, D. Neher, M. Stolterfoht, T. Unold, V. Getautis, S. Albrecht, *Science* **2020**, *370*, 1300.

[42] S. Gharibzadeh, P. Fassl, I. M. Hossain, P. Rohrbeck, M. Frericks, M. Schmidt, T. Duong, M. R. Khan, T. Abzieher, B. A. Nejand, F. Schackmar, O. Almora, T. Feeney, R. Singh, D. Fuchs, U. Lemmer, J. P. Hofmann, S. A. L. Weber, U. W. Paetzold, *Energy Environ. Sci.* **2021**, *14*, 5875.

[43] M. Roß, S. Severin, M. B. Stutz, P. Wagner, H. Köbler, M. Favin-Lévêque, A. Al-Ashouri, P. Korb, P. Tockhorn, A. Abate, B. Stannowski, B. Rech, S. Albrecht, *Adv. Energy Mater.* **2021**, *11*, 2101460.

[44] F.-M. Raoult, *J. Phys. Théor. Appl.* **1889**, *8*, 5.

[45] G. C. Fonger, *Toxicology* **1995**, *103*, 137.

[46] G. C. Fonger, P. Hakkinen, S. Jordan, S. Publicker, *Toxicology* **2014**, *325*, 209.

[47] H. Zhang, K. Darabi, N. Y. Nia, A. Krishna, P. Ahlawat, B. Guo, M. H. S. Almalki, T. Sen Su, D. Ren, V. Bolnykh, L. A. Castriotta, M. Zendehdel, L. Pan, S. S. Alonso, R. Li, S. M. Zakeeruddin, A. Hagfeldt, U. Rothlisberger, A. Di Carlo, A. Amassian, M. Grätzel, *Nat. Commun.* **2022**, *13*, 89.

[48] S. Rahimnejad, A. Kovalenko, S. M. Forés, C. Aranda, A. Guerrero, *ChemPhysChem* **2016**, *17*, 2795.

[49] O. Shargaieva, H. Näsström, J. A. Smith, D. Többens, R. Munir, E. Unger, *Mater. Adv.* **2020**, *1*, 3314.

[50] J. C. Hamill, J. Schwartz, Y.-L. Loo, *ACS Energy Lett.* **2018**, *3*, 92.

[51] G. Gritzner, S. Sperker, *J. Solution Chem.* **1988**, *17*, 1133.

[52] K. W. Lau, M. H. Aron, M. H. J. Yen, E. Y. Fung, S. Grzybicki, R. Matamoros, J. C. Curtis, *Inorg. Chim. Acta* **1994**, *226*, 137.

[53] A. S. Tutantsev, N. N. Udalova, S. A. Fateev, A. A. Petrov, W. Chengyuan, E. G. Maksimov, E. A. Goodilin, A. B. Tarasov, *J. Phys. Chem. C* **2020**, *124*, 11117.

[54] C. M. Hansen, *Hansen Solubility Parameters*, CRC Press, Boca Raton, FL **2007**.

[55] A. Sharenko, C. Mackeen, L. Jewell, F. Bridges, M. F. Toney, *Chem. Mater.* **2017**, *29*, 1315.

[56] J. Kim, B. Park, J. Baek, J. S. Yun, H.-W. Kwon, J. Seidel, H. Min, S. Coelho, S. Lim, S. Huang, K. Gaus, M. A. Green, T. J. Shin, A. W. Y. Ho-baillie, M. G. Kim, S. Il Seok, *J. Am. Chem. Soc.* **2020**, *142*, 6251.

[57] Y. Yu, F. Zhang, T. Hou, X. Sun, H. Yu, M. Zhang, *Sol. RRL* **2021**, *5*, 2100386.

[58] O. Almora, D. Baran, G. C. Bazan, C. Berger, C. I. Cabrera, K. R. Catchpole, S. Erten-Ela, F. Guo, J. Hauch, A. W. Y. Ho-Baillie, T. J. Jacobsson, R. A. J. Janssen, T. Kirchartz, N. Kopidakis, Y. Li, M. A. Loi, R. R. Lunt, X. Mathew, M. D. McGehee, J. Min, D. B. Mitzi, M. K. Nazeeruddin, J. Nelson, A. F. Nogueira, U. W. Paetzold, N. Park, B. P. Rand, U. Rau, H. J. Snaith, E. Unger, et al., *Adv. Energy Mater.* **2021**, *11*, 2002774.

[59] N. K. Noel, S. N. Habisreutinger, B. Wenger, M. T. Klug, M. T. Hörantner, M. B. Johnston, R. J. Nicholas, D. T. Moore, H. J. Snaith, *Energy Environ. Sci.* **2017**, *10*, 145.

[60] A. J. Ramadan, N. K. Noel, S. Fearn, N. Young, M. Walker, L. A. Rochford, H. J. Snaith, *Chem. Mater.* **2018**, *30*, 7737.

[61] T. Baikie, Y. Fang, J. M. Kadro, M. Schreyer, F. Wei, S. G. Mhaisalkar, M. Graetzel, T. J. White, *J. Mater. Chem. A* **2013**, *1*, 5628.

[62] P. Scherrer, *Math. Kl.* **1918**, *2*, 98.

[63] A. S. Thind, X. Huang, J. Sun, R. Mishra, *Chem. Mater.* **2017**, *29*, 6003.

[64] J. Cao, X. Jing, J. Yan, C. Hu, R. Chen, J. Yin, J. Li, N. Zheng, *J. Am. Chem. Soc.* **2016**, *138*, 9919.

[65] A. A. Petrov, I. P. Sokolova, N. A. Belich, G. S. Peters, P. V. Dorovatovskii, Y. V. Zubavichus, V. N. Khrustalev, A. V. Petrov, M. Grätzel, E. A. Goodilin, A. B. Tarasov, *J. Phys. Chem. C* **2017**, *121*, 20739.

[66] T. Su, X. Li, Y. Zhang, F. Zhang, Z. Sheng, *Phys Chem Chem Phys* **2017**, *19*, 13147.

[67] L. Tian, W. Zhang, Y. Huang, F. Wen, H. Yu, Y. Li, Q. Wang, C. Peng, Z. Ma, T. Hu, L. Du, M. Zhang, *ACS Appl. Mater. Interfaces* **2020**, *12*, 29344.

[68] S. Moghadamzadeh, I. M. Hossain, M. Jakoby, B. Abdollahi Nejand, D. Rueda-Delgado, J. A. Schwenzer, S. Gharibzadeh, T. Abzieher, M. R. Khan, A. A. Haghighirad, I. A. Howard, B. S. Richards, U. Lemmer, U. W. Paetzold, *J. Mater. Chem. A* **2020**, *8*, 670.

[69] M. E. O'Kane, J. A. Smith, T. I. Alanazi, E. J. Cassella, O. Game, S. van Meurs, D. G. Lidzey, *ChemSusChem* **2021**, *14*, 2537.

[70] X. Wang, Y. Fan, L. Wang, C. Chen, Z. Li, R. Liu, H. Meng, Z. Shao, X. Du, H. Zhang, G. Cui, S. Pang, *Chem* **2020**, *6*, 1369.

[71] C. Bracher, B. G. Freestone, D. K. Mohamad, J. A. Smith, D. G. Lidzey, *Energy Sci. Eng.* **2018**, *6*, 35.

[72] B. Wang, Z. G. Zhang, S. Ye, H. Rao, Z. Bian, C. Huang, Y. Li, *J. Mater. Chem. A* **2016**, *4*, 17267.

[73] F. Ali, C. Roldán-Carmona, M. Sohail, M. K. Nazeeruddin, *Adv. Energy Mater.* **2020**, *10*, 2002989.

[74] P. J. Hotchkiss, S. C. Jones, S. A. Paniagua, A. Sharma, B. Kippelen, N. R. Armstrong, S. R. Marder, *Acc. Chem. Res.* **2012**, *45*, 337.

[75] P. B. Paramonov, S. A. Paniagua, P. J. Hotchkiss, S. C. Jones, N. R. Armstrong, S. R. Marder, J.-L. Brédas, *Chem. Mater.* **2008**, *20*, 5131.

[76] S. A. Paniagua, E. L. Li, S. R. Marder, *Phys. Chem. Chem. Phys.* **2014**, *16*, 2874.

[77] G. Ashiotis, A. Deschildre, Z. Nawaz, J. P. Wright, D. Karkoulis, F. E. Picca, J. Kieffer, *J. Appl. Crystallogr.* **2015**, *48*, 510.

2203468 (14 of 14)